OPTICS

Photonic Floquet Landau-Zener tunneling and temporal beam splitters

Shulin Wang[1], Chengzhi Qin[1]*, Lange Zhao[1], Han Ye[1], Stefano Longhi[2,3]*, Peixiang Lu[1,4]*, Bing Wang[1]*

Landau-Zener tunneling (LZT), i.e., the nonadiabatic transition under strong parameter driving in multilevel systems, is ubiquitous in physics, providing a powerful tool for coherent wave control both in quantum and classical systems. While previous works mainly focus on LZT between two energy bands in time-invariant crystals, here, we construct synthetic time-periodic temporal lattices from two coupled fiber loops and demonstrate dc- and ac-driven LZTs between periodic Floquet bands. We show that dc- and ac-driven LZTs display distinctive tunneling and interference characteristics, which can be harnessed to realize fully reconfigurable LZT beam splitter arrangements. As a potential application to signal processing, we realize a 4-bit temporal beam encoder for classical light pulses using a reconfigurable LZT beam splitter network. Our work introduces and experimentally demonstrates a new class of reconfigurable linear optics circuits harnessing Floquet LZT, which may find versatile applications in temporal beam control, signal processing, quantum simulations, and information processing.

INTRODUCTION

Adiabaticity is a basic concept in many disciplines of science, which implies that a system would stay in its slowly evolving initial state when subject to a sufficiently slow parameter change (*1*). The breakdown of adiabaticity would lead to many observable phenomena, among which the most prominent signature is the Landau-Zener tunneling (LZT) effect (*2*, *3*), which manifests as a transition between two instantaneous energy levels at an avoided crossing point under strong external driving. LZT has a broad impact in different areas of physics and has been observed in several systems, including Bose-Einstein condensate (*4*, *5*), semiconductor superlattices (*6*, *7*), superconducting qubits (*8*–*10*), and optical waveguide arrays (*11*–*17*). LZT is also at the heart of the Schwinger pair production in quantum electrodynamics, i.e., the creation of matter from vacuum by an extremely strong electric field (*18*), and closely related to the Kibble-Zurek theory of the topological defect production in nonequilibrium phase transitions (*19*). Owing to its characteristic wave packet splitting nature, LZT has been exploited for developing many applications, ranging from coherent matter-wave control (*20*–*22*) and quantum computing (*8*–*10*) to LZT interferometry (*9*) and amplitude spectroscopy of artificial solid-state atoms (*23*).

Although LZT interferometry is known since more than two decades, it is only quite recently that it became fully accessible and useful for coherently manipulating a growing number of physical systems (*9*). Traditionally, LZT and LZT interferometry focus on multilevel (or multiband) systems with a static Hamiltonian, i.e., with continuous translational symmetry in time, where a slowly driving parameter can induce LZT among the various levels. For example, in solid-state systems, application of an electric field can induce the LZT of Bloch electrons between valence and conduction bands (*6*, *7*). In contrast to the traditional time-invariant crystals described by static Hamiltonians, a class of Floquet systems with time-periodic Hamiltonians have also attracted intensive attentions due to their versatilities in engineering Floquet bands (*24*–*26*). Floquet systems display some exotic properties, such as the anomalous Floquet topological insulators (*24*, *27*) and time crystals (*28*, *29*), which are rooted in the unique features of the periodically repeated quasi-energy band structures of Floquet systems. Recently, the concept of Floquet LZT, i.e., LZT between Floquet states in time-periodic systems, has been introduced (*30*–*33*) to explain dynamical features of laser-driven matter (*31*, *32*) and space-time crystals (*33*), with the observation of LZT in quantum walks under a dc field (*34*, *35*) and potential applications to quantum ratchets (*30*). However, the rich tunneling features of Floquet LZT and the realization of complex photonic circuits based on cascaded LZT beam splitter arrangements remain largely elusive in experiments.

In this work, we experimentally demonstrate Floquet LZT and fully reconfigurable LZT beam splitter arrangements in synthetic photonic temporal lattices, providing a feasible platform for controllable coherent wave manipulation of classical and quantum light. As a potential application to signal processing and routing, we design and realize a temporal beam encoder (*36*–*38*) harnessing the fully reconfigurability of the LZT beam splitter arrangement. Our photonic system consists of a mesh-type temporal lattice that is constructed by mapping from a coupled fiber-loop circuit (*39*–*49*). This system has been proved as an ideal platform in the synthetic time dimension to emulate a series of coherent spatial transport dynamics. For instance, by applying linearly varying phase modulations into the fiber loops, an effective dc-driving electric field for photons can be created and the corresponding Bloch oscillations (BOs) have been observed in the temporal lattice with gain and loss (*40*, *41*). More recently, by constructing an ac-driving electric field via sinusoidally varying phase modulations, high-order dynamic localizations have also been observed, based on which a

[1]Wuhan National Laboratory for Optoelectronics and School of Physics, Huazhong University of Science and Technology, Wuhan 430074, China. [2]Dipartimento di Fisica, Politecnico di Milano, Piazza Leonardo da Vinci 32, I-20133 Milano, Italy. [3]IFISC (UIB-CSIC), Instituto de Fisica Interdisciplinar y Sistemas Complejos, E-07122 Palma de Mallorca, Spain. [4]Hubei Key Laboratory of Optical Information and Pattern Recognition, Wuhan Institute of Technology, Wuhan 430205, China.
*Corresponding author. Email: qinchengzhi@hust.edu.cn (C.Q.); stefano.longhi@polimi.it (S.L.); lupeixiang@hust.edu.cn (P.L.); wangbing@hust.edu.cn (B.W.)

highly tunable temporal cloaking scheme was demonstrated (*48*). Such previous works mainly focused on transport dynamics with well-preserved adiabaticity, the effects arising from nonadiabaticity being fully neglected. However, the mesh-type synthetic temporal lattice is a very natural Floquet system, making it a promising platform to demonstrate nonadiabatic dynamics and Floquet LZT interferometry.

To realize Floquet LZT, we first create artificial electric fields in the lattice by applying phase modulations in the two coupled fiber loops. Unlike previous works on electric quantum walks (*34*, *35*), we realize both dc- and ac-driven regimes, which is essential for the design of reconfigurable LZT beam splitter arrangements. The dc- and ac-driven dynamics gives rise to distinct beam interference features for the cascaded LZT beam splitters, i.e., the ac-driven case can facilitate beam splitting by suppressing the beam interference and concentration as compared to the dc-driven case. By combining both dc- and ac-driven LZTs, coherent and reconfigurable wave control can be realized. We demonstrate the potentiality of the LZT beam splitter arrangement with combined dc and ac driving in signal processing and routing by designing a temporal beam encoding system with full-tunable digital outputs. In our experiment, we demonstrate a 4-bit digital beam encoder and achieve the digital bit generation from the formats 0001 to 1111 by appropriately tuning the driving. Our experimental findings provide full insights into Floquet LZT interferometry and demonstrate its potentiality for the realization of complex and fully reconfigurable linear optic circuits, which holds great promise in applications to coherent wave control, signal processing and routing, quantum simulations, and information processing.

RESULTS

Construction of Floquet temporal lattices

A Floquet temporal lattice can be constructed by mapping from a light pulse evolution in two coupled fiber loops with slightly different lengths, as shown in Fig. 1A. To feed the coupled fiber-loop circuit, a light pulse is injected into one of the loops. After passing through the central coupler connecting the two loops, the initial pulse splits into two parts and enters the short and long loops. Because of the length difference between two loops, the pulse circulating in the longer loop is relatively delayed compared to that in the shorter one, giving rise to the successive pulse separation and recombination in the time domain. As the circulation step increases, the initial pulse evolves into a pulse train locating at a series of uniformly distributed time slots. The circulation step "m" and the site of time slot "n" can be mapped conceptually into the longitudinal and transverse axes of a "mesh-type" temporal lattice (*39*–*41*). Then, light propagations in the short and long loops correspond to the leftward and rightward hopping in the lattice. Note that, because of the discrete nature in the time-evolution direction m, this system manifests itself as a discrete Floquet temporal lattice.

To induce LZT in the Floquet lattice, an essential prerequisite is to introduce an artificial electric field into the lattice to drive the Bloch momentum passing through the lattice's bandgap. This can be achieved by applying opposite, step-dependent phase modulations of $\phi_u(m)$ and $\phi_v(m) = -\phi_u(m)$ in the short and long loops. Then, light hopping in the leftward and rightward directions can acquire opposite phase shifts $\pm\phi_u(m)$, which imparts an effective gauge potential $A_{\text{eff}}(m) = -\phi_u(m)$ into the lattice through Peierls substitution (*50*–*52*). Because the evolution step m plays the role of time "t," this time-varying gauge potential can yield an effective electric field $E_{\text{eff}}(m) = -dA_{\text{eff}}(m)/dm = d\phi_u(m)/dm$ with rather arbitrary dependence on the step index m, i.e., not just a dc field as in previous works (*34*, *35*). To fully exploit the potentialities of Floquet LZT interferometry in coherent wave packet control, in this study, we choose two typical types of phase modulations: the linear-varying $\phi_u(m) = \alpha m$ and the periodically oscillating $\phi_u(m) = -\Delta\phi\cos(\omega m + \phi)$, which can generate a dc- and an ac-driving electric field

$$E_{\text{eff}}(m) = \begin{cases} \alpha, & (\text{dc}) \\ \omega\Delta\phi\sin(\omega m + \varphi) & (\text{ac}) \end{cases} \tag{1}$$

where α is the gradient of linear-varying phase modulation; $\Delta\phi$, ω, and ϕ are the amplitude, frequency, and initial phase of harmonic oscillating phase modulation, respectively. A combination of the two driving fields will be also considered.

Under the driving of a dc or an ac electric field, the pulse evolution in the Floquet temporal lattice is governed by the following map (*39*–*41*, *48*)

$$\begin{cases} u_n^m = (\sqrt{1-T} \times u_{n+1}^{m-1} + i\sqrt{T} \times v_{n+1}^{m-1})e^{i\phi_u(m)} \\ v_n^m = (i\sqrt{T} \times u_{n-1}^{m-1} + \sqrt{1-T} \times v_{n-1}^{m-1})e^{-i\phi_u(m)} \end{cases} \tag{2}$$

where u_n^m and v_n^m denote the pulse complex amplitudes in short and long loops at the lattice grid (m, n). T is the transmittance of the central coupler, with T:$(1 - T)$ being its coupling ratio that ranges from 0:1 to 1:0. The phase $\phi_u(m)$ is assumed to vary slowly with step number m, so that the entire dynamics occurs on two time scales: a "fast" time scale, defined by the discrete evolution from $(m - 1)$ to m with an instantaneous constant phase $\phi_u(m)$, and a "slow" time scale defined by the characteristic time where $\phi_u(m)$ significantly changes. The instantaneous eigen Floquet-Bloch modes supported by the lattice are $(u_n^m, v_n^m)^{\text{T}} = (U, V)^{\text{T}} e^{iQn} e^{i\theta m}$, where $(U, V)^{\text{T}}$ is the eigenvector, Q and θ are the transverse Bloch momentum and longitudinal propagation constant, respectively. Substituting eigen mode into Eq. 2, we can obtain the Floquet band structure

$$\theta_{l,\pm}[Q(m)] = \pm\arccos[\sqrt{1-T}\cos Q(m)] + 2l\pi \tag{3}$$

where $Q(m) = Q + \phi_u(m)$ is the slowly varying Bloch momentum, l is an integer denoting the Floquet band index, and "±" represent the positive and negative minibands within one Floquet period $[-\pi + 2l\pi, \pi + 2l\pi]$. As illustrated in Fig. 1 (B and C), a series of Floquet bands are periodically distributed both in the Q and θ axes. In particular, the two mini-bands within each Floquet period is separated by a bandgap $\theta_g = \min(|\theta_+ - \theta_-|) = 2\arcsin(T^{1/2})$, which is uniquely determined by the transmittance T. Meanwhile, the adjacent Floquet periods are also separated by this same bandgap. As we will show below, a Bloch wave packet will show LZT when approaching each of these band gaps under dc- or ac-driving electric field, which is referred to as Floquet LZT. Note that LZT between adjacent Floquet periods is unique to our Floquet lattice and has no counterpart to traditional time-invariant systems.

Theoretical model of dc- and ac-driven LZT

In this section, we will investigate the unique features of Floquet LZT under a dc- or an ac-driving electric field by comparing their respective tunneling time and probability, as well as their distinct

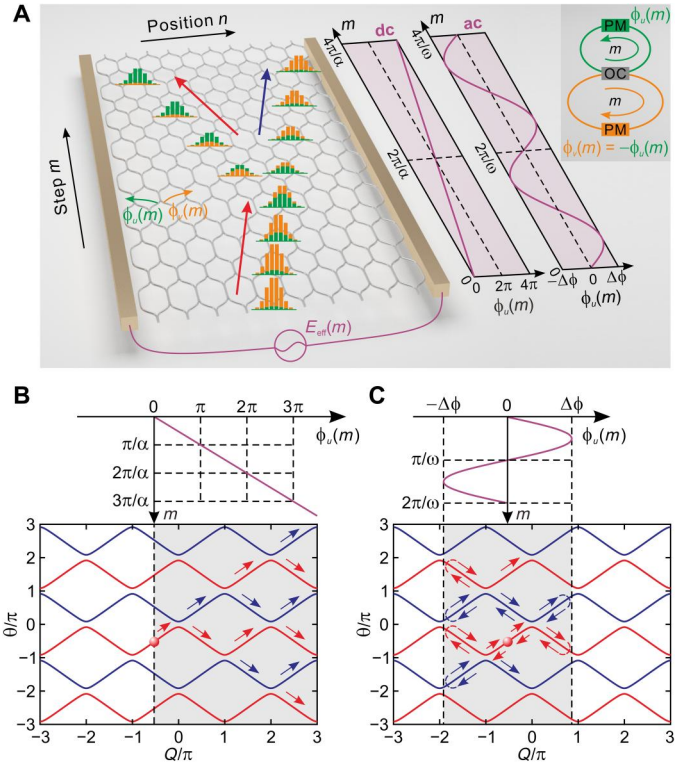

Fig. 1. Principle of dc- and ac-driven LZTs in synthetic temporal lattices. (**A**) Schematic of a synthetic temporal mesh lattice created from two coupled fiber loops as shown by the inset figure. The opposite time-varying phase modulations $\phi_u(m)$ and $\phi_v(m)$ are introduced to generate the nonreciprocal phase acquisitions during the leftward and rightward hopping, which lead to the artificial ac and dc electric fields. The wave packet splitting indicates the occurrence of LZT. The green and orange colors correspond to the short and long loops, respectively. (**B**) Band structure of dc-driven synthetic temporal lattice. The negative and positive band branches are denoted by red and blue solid curves, respectively. Here, a Bloch wave packet is excited at the negative band branch, which is represented by the red ball. Under the dc driving, the wave packet's Bloch momentum is shifted along the transverse axis of band structure with a constant velocity α. During shifting, the packet's splitting and movement at the Floquet band structure are reflected by the arrows. (**C**) Band structure of ac-driven temporal lattice. Under the ac driving, the Bloch momentum exhibits periodic oscillations within a finite range of $2\Delta\phi$ and with a period of $M_{ac} = 2\pi/\omega$.

wave packet interference characteristics for the cascaded tunneling events. First, for a dc-driven electric field $E = \alpha$, the Bloch momentum exhibits a linear sweep across the Brillouin zone at a constant rate α, i.e., $Q(m) = Q + \alpha m$, as shown in Fig. 1B. When approaching each of the band gaps at the Brillouin zone's centers or edges, the adjacent bands are almost in touch and LZT will take place. The explicit tunneling time instant and probability can be obtained by applying the Landau-Zener formula involving the concepts of instantaneous adiabatic and diabatic energy levels (*9*). Substituting $Q(m)$ into the Floquet band structure of Eq. 3, we can obtain the instantaneous adiabatic energy levels

$$\theta_{l,\pm}(m) = \theta_{l,\pm}[Q(m)] = \pm\arccos[\sqrt{1-T}\cos(Q+\alpha m)] + 2l\pi \quad (4)$$

Furthermore, by taking the limit with $T = 0$, i.e., the complete decoupling between the two fiber loops, we can also get the instantaneous diabatic energy levels

$$\theta_{d,\pm}(m) = \pm(Q+\alpha m) + 2l\pi \quad (5)$$

As also shown in Fig. 2A, the crossing of diabatic energy levels with $\theta_{d,+}(M_i) = \theta_{d,-}(M_i)$ (dashed curves) can predict the avoided crossing of the adiabatic levels (solid curves), and hence the time instant of the *i*th LZT event in the *m* axis

$$M_i = \frac{i\pi - Q}{\alpha} \quad (6)$$

Hereafter, we assume that the initial Bloch momentum satisfies the constraint $0 < Q < \pi$. The dc-driving electric field α thus gives rise to uniformly distributed tunneling positions spaced by $\pi/|\alpha|$ in the *m* axis. Meanwhile, the tunneling probability P_i of LZT can be determined by the level velocity v_{level} (*53*, *54*) of the diabatic levels, $v_{level} = d|\theta_{d,+}(m) - \theta_{d,-}(m)|/dm = 2|\alpha|$. By applying the Landau-Zener formula (*2*, *9*), we can find that the dc-driving electric field

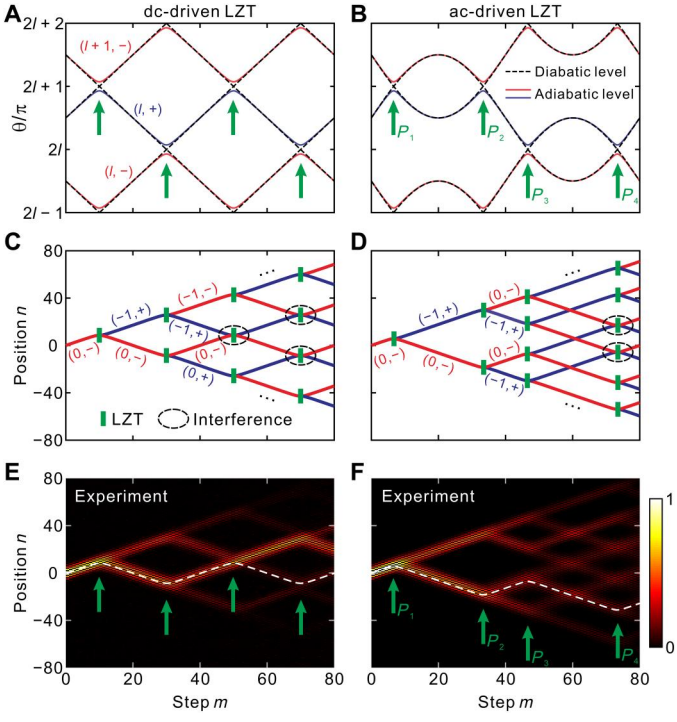

Fig. 2. Comparison between dc- and ac-driven LZT effects. (**A** and **B**) Instantaneous energy levels varying with step *m* under ac and dc driving. The diabatic and adiabatic levels are denoted by the dashed and solid curves, respectively. The degenerate point of adjacent diabatic levels is indicated by the green arrows, which predicts the tunneling time of the LZT. (**C** and **D**) Trajectories of wave packets under dc and ac driving, respectively. For positive and negative band branches, the corresponding wave packet trajectories are denoted by the blue and red solid lines. The green blocks indicate the positions of LZT effects. The dashed ellipses reflect the interference at LZT. (**E** and **F**) Corresponding measured pulse intensity evolutions. The white dashed curve indicates the trajectory of survival wave packet.

yields a constant tunneling probability

$$P_i = \exp\left(\frac{-2\pi T}{v_{\text{level}}}\right) = \exp\left(\frac{-\pi T}{|\alpha|}\right) \quad (7)$$

Let us now consider the Floquet LZT under ac-driving electric field, where the Bloch momentum sinusoidally varies with the step m, i.e., $Q(m) = Q - \Delta\phi\cos(\omega m + \phi)$, as illustrated in Fig. 1C. Different from the dc-driven LZT with an infinitely extended Bloch momentum, the Bloch momentum under the ac driving is limited within the interval of $[Q - \Delta\phi, Q + \Delta\phi]$ and manifests reflections when reaching the boundaries of the interval. The adiabatic energy levels under the ac-driving electric field read

$$\theta_{l,\pm}(m) = \pm\arccos\{\sqrt{1-T}\cos[Q - \Delta\phi\cos(\omega m + \varphi)]\} + 2l\pi \quad (8)$$

which correspond to the diabatic energy levels

$$\theta_{d,\pm}(m) = \pm[Q - \Delta\phi\cos(\omega m + \varphi)] + 2l\pi \quad (9)$$

Letting $\theta_{d,+}(M_i) = \theta_{d,-}(M_i)$, we can also obtain the ith tunneling position for the ac-driven case

$$M_i = \pm\frac{1}{\omega}\arccos\frac{Q + R\pi}{\Delta\phi} + \frac{1}{\omega}(2S\pi - \varphi) \quad (10)$$

where the arccos function is a monodrome function with a range $[0, \pi]$, $|(Q + R\pi)/\Delta\phi| \leq 1$, and R and S are integers. The LZT occurs periodically with the ac-driving period $2\pi/\omega$. Different from the above dc-driven LZT case, the ac-driven LZT exhibits a nonuniform distribution of tunneling positions within each driving period, as shown in Fig. 2B. The corresponding level velocity under ac driving is given by $v_{\text{level}} = d|\theta_{d,+}(m) - \theta_{d,-}(m)|/dm = 2|\Delta\phi\omega\sin(\omega M_i + \phi)|$, yielding a nonuniform tunneling probability

$$P_i = \exp\left(\frac{-2\pi T}{v_{\text{level}}}\right) = \exp\left(\frac{-\pi T}{|\Delta\phi\omega\sin(\omega M_i + \varphi)|}\right) \quad (11)$$

Apart from the differences in the tunneling time and probability for each LZT event, the cascaded LZT process under dc or ac driving also manifests different interference characteristics owing to their distinct evolution dynamics outside each LZT event. For the dc-driven case, the wave packet manifests BOs between adjacent LZT events, which is referred to as Bloch-Zener oscillation (*13*, *15*–*17*, *20*, *21*, *35*). This process can be visualized in Fig. 2C, where an initial wave packet belonging to the negative branch is launched into the lattice. After the first LZT event, the packet splits into two parts, which will exhibit the second LZT after half of Bloch period $M_{\text{BO}}/2$. Because of the periodic nature of BOs, the two split wave packets will meet and exhibit LZT again after a complete Bloch period M_{BO}, showing the inevitable beam interference. The interference can be constructive or destructive, making the packet concentrated mainly into one beam branch, which will, in turn, suppress the successive beam splitting. By contrast, for the ac-driving case, the wave packet exhibits no periodically oscillatory motion of BOs but directional transport between LZT events. As shown in Fig. 2D, the split wave packets after twice LZTs cannot meet because of their opposite group velocities (see note S1). As a result, the ac-driven LZT can enhance beam splitting by suppressing light concentration into one branch. After one driving period of $M_{\text{ac}} = 2\pi/\omega$, there exists a portion of wave packet staying in original band branch and experiencing no LZT. The ratio of this remaining part is dubbed survival probability, which can be calculated by

$$P_{\text{survival}} = \prod_{i=1}^{K}(1 - P_i) \quad (12)$$

where K is the total times of LZT events within a driving period M_{ac} and $\prod$ denotes the multiplicative calculation. The above relation holds provided that, along the path of the original branch, interference arising from recombining wave packets does not occur (as in the example shown in Fig. 2D) or it can be neglected. The effective tunneling probability after one driving period of the ac field can thus be defined by

$$P_{\text{eff}} = 1 - P_{\text{survival}} = 1 - \prod_{i=1}^{K}(1 - P_i) \quad (13)$$

indicating that the increase of tunneling probability of each LZT event can boost the effective tunneling probability in a complete driving period. For the dc-driven case interference effects at successive LZT events are important to determine the final effective tunneling probability (*9*), and thus, the simple form given by Eq. 13 cannot be used anymore. The cascading of LZT events, i.e., beam splitters, gives rise to many possible paths of the wave packet, which are arranged in regular or irregular trees, as shown in Fig. 2 (C and D). Owing to the almost linear dispersion relation of the quasi-energy bands in the Floquet synthetic lattice, the paths connecting the beam splitters in the tree are straight segments.

Experimental realization of dc- and ac-driven LZTs and tunable LZT temporal beam splitters

The LZT features for dc and ac driving have been experimentally verified on the basis of the coupled fiber-loop circuit. The schematic sketch of the experimental setup is shown in note S2. The average length and length difference of the two fiber loops are set as ~5 km and ~30 m, corresponding to a time step and time-slot delay of ~25 μs and ~75 ns, respectively. To create the synthetic temporal lattice, the time difference of fiber loops needs to be the same during the pulse circulations in the loops. In our experiments, each measurement that maps the pulse circulation into the evolution dynamics in the temporal lattice only lasts 2 to 3 ms. At such a relatively short time scale, the length difference of the two loops nearly remains unchanged, which satisfies the requirement for creating a stable temporal lattice. To feed the fiber loops, we prepare a pulse train with a Gaussian envelope, i.e., a wave packet, obtained from the evolution of a single ~100-ns-long light pulse (*42*, *48*). The required dc- or ac-driving electric field is introduced by inserting a phase modulator (PM) into the short fiber loop that is driven by an arbitrary waveform generator (AWG). The LZT processes are measured by recording the wave packet intensity evolutions tapered from the two fiber loops. Other details about the experimental setup and measurement method are provided in Materials and Methods and note S2.

In the experiment, we excite a wave packet with a Bloch momentum of $Q = \pi/2$ from the negative energy branch. Figure 2E displays the cascaded LZT process by choosing a dc-driving field with $\alpha = \pi/20$, which corresponds to a Bloch period $M_{\text{BO}} = 2\pi/\alpha = 40$ steps. The transmittance of the coupler is fixed at $T = 0.05$. As predicted by the diabatic levels in Fig. 2A, the impinging wave packet experiences four times of LZT at m = 10, 30, 50, and 70 steps within two

Bloch periods, which are accompanied by beam splitting for each LZT event and lastly give rise to a plenty of beam branches. Quite different from the ordinary two-band LZT with only one LZT event in one Bloch period, here, we have two LZT events in one period due to the additional LZT events occurring between adjacent Floquet bands. As a result, more times of beam splitting can be observed during the propagation while only two branches exist in the ordinary two-band LZT. Because of the presence of beam interference at intermediate LZT events, the light intensity will be mainly concentrated onto one of these branches.

For comparison, we also measure the wave packet dynamics for ac-driven LZT. The modulation amplitude, frequency, and initial phase of phase modulation are chosen as $\Delta\phi = \pi$, $\omega = \pi/40$, and $\phi = \pi/2$, respectively. As shown in Fig. 2F, the ac-driven LZT happens at $m = 7$, 33, 47, and 77 steps, which are nonuniformly distributed along the step m. At each LZT event, the wave packet splits equally into two parts due to the tunneling probability of $P_1 = P_2 = P_3 = P_4 = 0.5$. For most of LZT events, the split wave packets occupying the two bands show no overlapping and hence are free of beam interference. After the first three LZT events in one driving period, the incident wave packet equally splits into eight parts, showing more obvious light energy spreading than the dc-driven LZT. Because of the ability to be immune to beam interference, the ac-driven LZT lastly enhances the wave packet spreading into more branches and is thus more desirable for the multipath routing and time-division multiplexing applications. Note that, in our experiments, numerous low-intensity pulses arise during the cascaded LZT process, which can be easily affected by the noise from erbium-doped fiber amplifiers (EDFAs). Therefore, the valid evolution steps are about 150 to 200 in our practical experiments, above which the tree-like pulse evolution pattern will be unclear and deviate from the theoretical one. Within these valid evolution steps, typically several or a dozen periods of Bloch-Zener oscillations or LZT can be realized, which depend on the dc-driving amplitude or ac-driving frequency. Here, we mainly concentrate on the explicit wave packet's LZT dynamics, so we choose a quite large ac period and make it commensurate with lattice evolution period ($M_{ac} = 2\pi/\omega = 80$ steps). The discrete evolution dimension can be nearly regarded as a continuous one. For the commensurate ac modulation period, the Floquet spectrum is absolutely continuous, and we can avoid localization effects. However, we point out that, because we operate in the slow modulation regime, unlike (*34*), whether the ratio between the ac period and lattice evolution period is commensurate or not has little influence on the evolution dynamics in our operational conditions.

Then, we show how the tunneling probability of ac-driven LZT can be efficiently controlled by the driving amplitude $\Delta\phi$ and the coupler's transmittance T. As illustrated in Fig. 3A, the effective tunneling probability P_{eff} will increase with $\Delta\phi$ or decrease with T. For a sufficiently small value of $\Delta\phi$, the probability P_{eff} vanishes for an arbitrarily chosen T, indicating a threshold feature for the ac-driven LZT. Such a threshold feature is due to the finite range of Bloch momentum $[Q - \Delta\phi, Q + \Delta\phi]$ that can be reached under the ac driving. The explicit threshold for the driving amplitude is $\Delta\phi = |Q|$ or $|\pi - Q|$, as indicated by the spacing between the initial Bloch momentum Q and the LZT position at Brillouin zone's center or edge. More detailed discussion about the threshold feature of the ac-driven LZT is provided in note S3. On the other extreme, as $\Delta\phi$ is large enough, the effective tunneling probability P_{eff} is saturated to unity, corresponding to the complete tunneling after the driving period. Note that the dc-driven LZT exhibits no threshold feature because the wave packet can sweep the entire Brillouin zone for an arbitrary dc field strength α.

Besides controlling the effective tunneling probability, the ac-driving amplitude $\Delta\phi$ can also control the times of LZT events within one period. Figure 3B shows the diabatic and adiabatic energy levels for three typical values of $\Delta\phi = 0$, 4, and 7, which show the increase of LZT events by increasing $\Delta\phi$, as clearly marked by the green arrows. For $\Delta\phi = 0$, the energy levels become flat, and, hence, LZT is completely inhibited. Correspondingly, the input wave packet moves along a single trajectory with no beam splitting, as also verified by the measured pulse intensity evolutions in Fig. 3C. For $\Delta\phi = 4$ (Fig. 3D), there are four LZT events at step $m = 5$, 35, 45, and 75 with the same tunneling probabilities $P_1 = P_2 = P_3 = P_4 = 0.35$, yielding a final effective tunneling probability of $P_{eff} = 0.83$, i.e., with 17% light energy remaining in the original branch. By increasing $\Delta\phi$ to 7 (Fig. 3E), we observe eight times of LZT at $m = 3$, 9, 31, 37, 43, 49, 71, and 77 with $P_1 = P_4 = P_5 = P_8 = 0.56$ and $P_2 = P_3 = P_6 = P_7 = 0.46$ and larger effective tunneling probability of $P_{eff} = 0.997$. Accordingly, the input packet is totally tunneled into other Floquet bands, with almost no light energy remained in the original trajectory. The increase of tunneling events at a larger driving amplitude $\Delta\phi$ is due to the fact the wave packet passes through tunneling positions of Brillouin zone center or edge more frequently.

Last, we show that the tunneling probability of ac-driven LZT can also be manipulated by the bandgap of lattice, which is also clearly indicated by Eq. 11. Figure 3 (F to H) shows the pulse intensity evolutions for $T = 0.5$, 0.15, and 0.05. Here, the modulation amplitude is kept constant to the same value as in Fig. 3D, i.e., $\Delta\phi = 4$, so that the time instants and number of LZT events do not change as T is varied. For $T = 0.5$, we observe that the LZT is almost totally suppressed. While for $T = 0.15$, four times of LZT events happen with the corresponding tunneling probabilities being $P_1 = P_2 = P_3 = P_4 = 0.2$, corresponding to an effective tunneling probability of $P_{eff} = 0.58$. This effective tunneling probability can be further increased to $P_{eff} = 0.97$ by choosing $T = 0.05$, as clearly shown in Fig. 3H.

Demonstration of a temporal beam encoder in LZT circuits

The most prominent features of LZT are the wave packet splitting and interference dynamics, which are at the basis of major applications to tunable coherent wave splitting, quantum control, LZT interferometry, amplitude spectroscopy, etc. (*9*, *10*, *20*–*23*). In this section, we will exploit the beam splitting functionality offered by Floquet LZT in an extended form, combining suitably tailored dc and ac driving, to design a reconfigurable LZT beam splitter arrangement for temporal beam encoding. Typically, a temporal beam encoding system consists of cascaded beam splitters with their splitting ratio being full-range tunable, and the output ports should be unmovable to fix the positions of output beams. If we apply only dc driving, then the splitting ratio of beam splitter can only be tuned by the driving strength α. Nevertheless, the variation of α will also affect the packets' evolution trajectories and hence the output beam positions (see note S4 for more detailed discussion). On the other hand, if we use only ac driving, then the threshold feature will also limit its tunability. To break the above limitations of merely dc or ac driving, here, we propose a new design by applying a weak ac driving superimposed onto a biased dc driving: Using

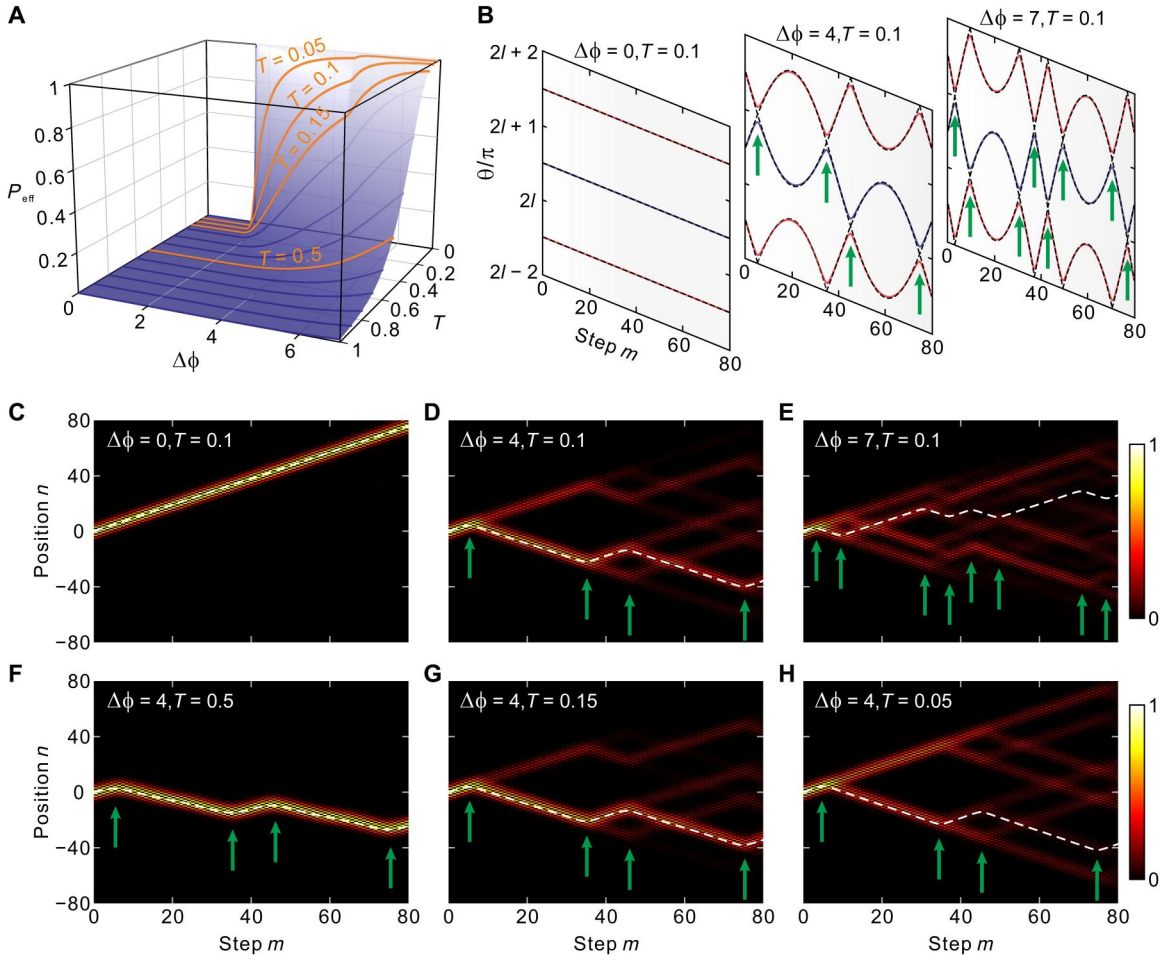

Fig. 3. Manipulation of ac-driven LZT. (**A**) Effective tunneling probability P_{eff} as a function of modulation amplitude Δϕ and coupler transmittance T. The effective tunneling probabilities for $T = 0.05$, 0.1, 0.15, and 0.5 are highlighted by orange color. (**B**) Instantaneous energy levels for Δϕ = 0, 4, and 7, where the coupler transmittance is $T = 0.1$. (**C** to **E**) Experimental results of pulse intensity evolutions as Δϕ = 0, 4, and 7. The coupler transmittance is $T = 0.1$. (**F** to **H**) Measured pulse intensity evolutions for $T = 0.5$, 0.15, and 0.05, where the modulation amplitude is Δϕ = 4.

such a combined driving scheme, we can successfully achieve a tunable beam encoder for signal processing applications (Fig. 4A). The combined driving field reads $E_{\text{eff}}(m) = \alpha + \omega\Delta\phi\sin(\omega m + \phi)$ and can be obtained from the phase modulation $\phi_u(m) = \alpha m - \Delta\phi\cos(\omega m + \phi)$. Under the combined driving, the adiabatic and diabatic levels are given by $\theta_{l,\pm}(m) = \pm\arccos\{(1 - T)^{1/2}\cos[Q + \alpha m - \Delta\phi\cos(\omega m + \phi)]\} + 2l\pi$ and $\theta_{d,\pm}(m) = \pm[Q + \alpha m - \Delta\phi\cos(\omega m + \phi)] + 2l\pi$. By using the criterion $\theta_{d,+}(M_i) = \theta_{d,-}(M_i)$ and level velocity $v_{\text{level}} = 2|\alpha + \Delta\phi\omega\sin(\omega M_i + \phi)|$, we can precisely obtain the tunneling time instants and tunneling probabilities and hence accurately design the beam encoder's specification. Note that, to construct a beam encoder without any diffraction spreading, we set the initial Bloch momentum as $Q = \pi/2$ with a vanishing diffraction coefficient $D_{\pm} = \partial^2\theta_{\pm}/\partial^2 Q = 0$.

For traditional dc-driven case, the first LZT happens at $m = \pi/2\alpha$ with a tunneling probability $P_{\text{T}} = \exp(-\pi T/|\alpha|)$. When adding a resonant ac-driving electric field with its frequency and initial phase being $\omega = 2\alpha$ and $\phi = \pm\pi/2$, the tunneling time is still $m = \pi/2\alpha$. However, the field intensity becomes $E_{\text{eff}} = \alpha \mp \omega\Delta\phi$ for $\phi = \pm\pi/2$ at the LZT, which gives rise to an increased level velocity $v_{\text{level}} = 2|\alpha + \omega\Delta\phi|$ and a decreased one $v_{\text{level}} = 2|\alpha - \omega\Delta\phi|$. By inserting the level velocity into the Landau-Zener formula, we can get an ac-modified tunneling probability

$$P_{\text{T}} = \exp\left(\frac{-\pi T}{|\alpha \mp \omega\Delta\phi|}\right) \tag{14}$$

where "∓" correspond to the initial phases $\phi = \pm\pi/2$. Figure 4B shows the tunneling probability P_{T} as a function of ac-modulation amplitude Δϕ, where the dc field intensity and the ac field frequency are set as $\alpha = \pi/12$ and $\omega = \pi/6$, respectively. Meanwhile, the coupler transmittance is fixed at $T = 0.05$. As Δϕ increases, P_{T} increases for $\phi = -\pi/2$ and decreases for $\phi = \pi/2$, which coincides well with the prediction in Eq. 14. By varying Δϕ and ϕ, a broad tuning range between $P_{\text{T}} = 0.22$ and $P_{\text{T}} = 0.68$ is achieved in experiment, while the only dc-driving case corresponds to a fixed tunneling probability $P_{\text{T}} = 0.55$. For examples, in Fig. 4 (C and D), we show the energy levels and measured pulse intensity evolutions with different Δϕ and ϕ. For the ac-driving-free case of Δϕ = 0 (Fig. 4, Ci and Di), one can observe the LZT-induced beam splitting at $m = 6$, with a measured tunneling probability of $P_{\text{T}} = 0.55$. Note that, to ensure

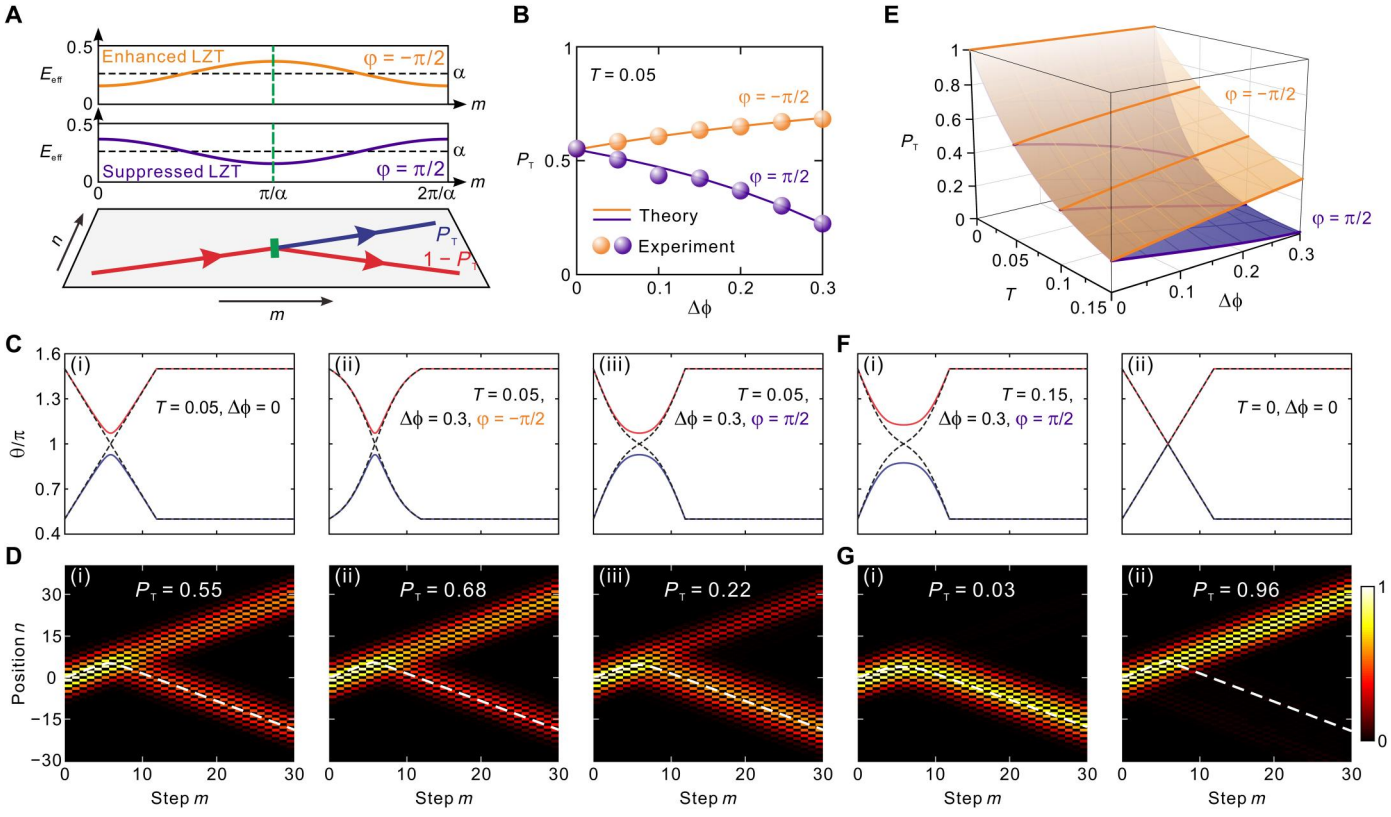

Fig. 4. Full-range tunable beam splitting enabled by ac-dc driving. (**A**) Schematic of ac-dc–driven beam splitter. The red and blue beams represent the wave packets at the negative and positive bands, respectively. The inset figures at the top display the combined electric fields for $\phi = \pm\pi/2$, which lead to the suppressed and enhanced LZT effects, respectively. (**B**) Tunneling probabilities P_T versus ac-modulation amplitude $\Delta\phi$. The tunneling probabilities with phases $\phi = \pm\pi/2$ are indicated by the purple and orange colors. The coupler transmittance is set as $T = 0.05$. (**C**) Instantaneous energy levels under different values of $\Delta\phi$: (i) ac-free case; (ii) enhanced LZT with $\phi = -\pi/2$ and (iii) the suppressed LZT with $\phi = \pi/2$, where $\Delta\phi = 0.3$. (**D**) Corresponding measured pulse intensity evolutions. (**E**) Tunneling probabilities P_T versus modulation amplitude $\Delta\phi$ and coupler transmittance T. (**F**) Instantaneous energy levels under different tuning of $\Delta\phi$ and T: (i) totally suppressed LZT as the coupler transmittance T is increased to 0.15, and (ii) complete tunneling arising from the close of the bandgap as $T = 0$. (**G**) Corresponding measured pulse intensity evolutions.

the distinct separation of the wave packets, here, we remove the external driving after $m = 12$ and make the split wave packets to undergo directional transport in the next 18 steps. When adding an ac driving with $\Delta\phi = 0.3$ and $\phi = -\pi/2$, the energy levels vary much more rapidly at the tunneling time compared to the ac-free case (Fig. 4Cii). Accordingly, the theoretical tunneling probability is increased to $P_T = 0.69$, as also verified by the measured value $P_T = 0.68$. In the pulse dynamics illustrated in Fig. 4Dii, we can observe that the upper branch, i.e., the tunneled part, is obviously enhanced. If one switches the ac driving′s phase to $\phi = \pi/2$, then the level velocity will show a significant reduction (Fig. 4Ciii). The tunneled part will be highly suppressed with a reduced tunneling probability $P_T = 0.22$ (Fig. 4Diii).

By merely controlling the ac driving, the variation of tunneling probability P_T may be not large enough. To further extend the tuning range of P_T, we propose to change the coupler transmittance T. Figure 4E illustrates the tunneling probability P_T versus the coupler transmittance T and the ac-modulation amplitude $\Delta\phi$, indicating that the tunneling probability P_T is extended into a full range, i.e., from 0 to 1. Typically, a vanished probability P_T corresponds to the conditions $T = 0.15$, $\Delta\phi = 0.3$, and $\phi = \pi/2$, where the bandgap is enlarged compared to the case of $T = 0.05$ (Fig. 4Fi). Accordingly, the experimental results of Fig. 4Gi show that the upper branch nearly totally vanishes ($P_T = 0.03$) under such a tuning condition. On the contrary, tuning the coupler transmittance to the value $T = 0$ leads to the close of bandgap and thus the total tunneling ($P_T = 0.96$), as illustrated in Fig. 4 (Fii and Gii). Note that, in theory, the tunneling probability should be $P_T = 1$ for $T = 0$. Nevertheless, limited by the noise from optical amplifiers, it is very hard to obtain a vanishing optical signal at the original branch and observe a complete tunneling. Likewise, the measurement of the totally suppressed tunneling is also affected by the noise. In the above wave packet dynamics, one sees that the envelopes and transverse position of two output wave packets exhibit no change even if the ac driving and coupler transmittance are modified (see note S5). Therefore, the alignments of the beam splitter outputs are well preserved in our beam splitting scheme.

The direct application of the above fully tunable beam splitter is the digital beam encoding. As illustrated by Fig. 5A, we prepare a wave packet from the negative band as the input and place three beam splitters on the wave packet possible routes. Specifically, the first beam splitter is realized by applying ac-dc driving from $m = 0$ to $m = 12$, while the frequency of ac driving and the intensity of dc driving are chosen as $\omega = \pi/6$ and $\alpha = \pi/12$, respectively. Likewise, the LZT-induced beam splitting occurs at $m = 6$ with a full-range tunable tunneling probability P_{T1}. From $m = 12$ to $m = 46$, the

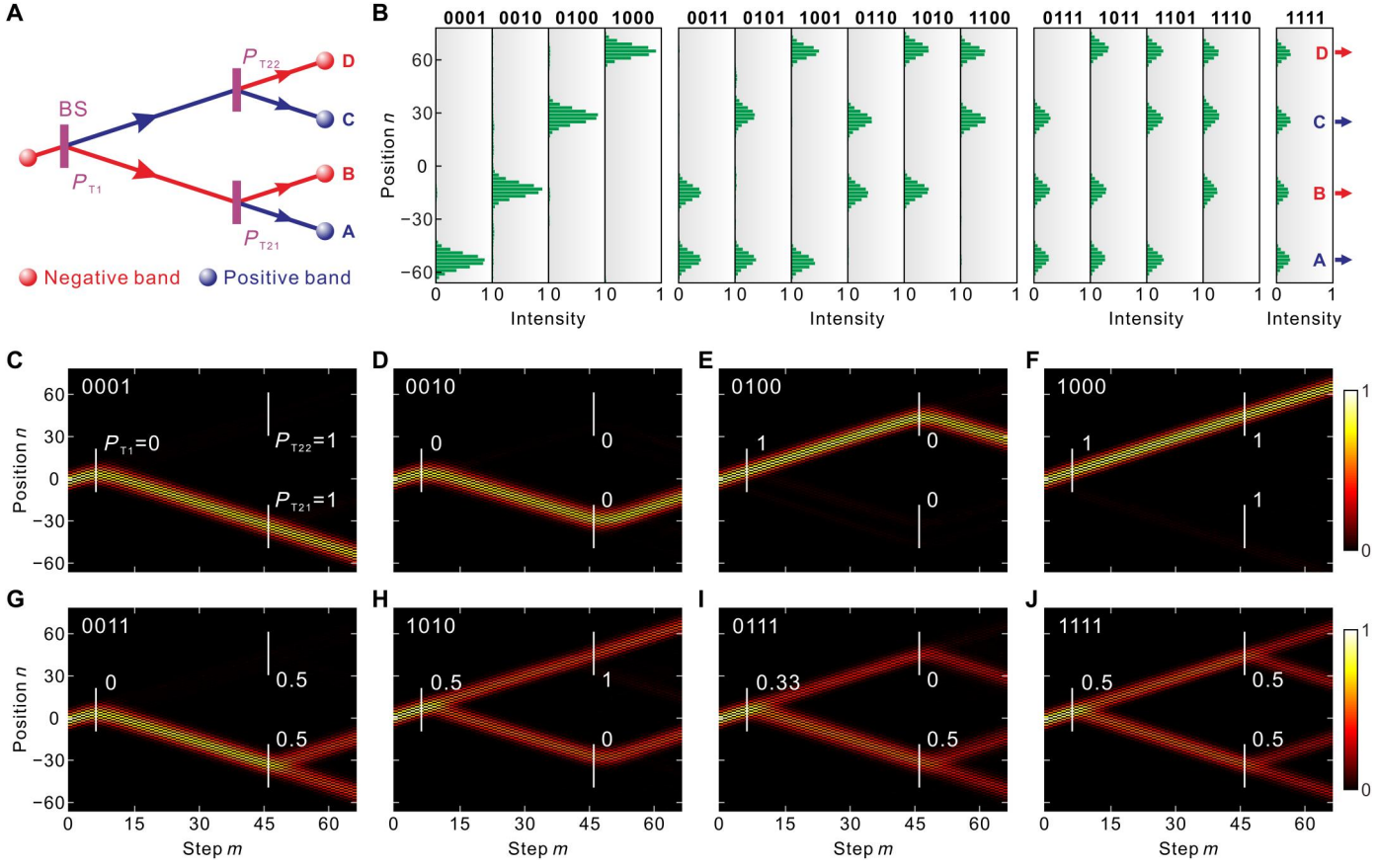

Fig. 5. Temporal beam encoding arising from cascaded beam splitters. (**A**) Schematic diagram of temporal beam encoding. Three full-range tunable beam splitters (BS) are placed at the paths of wave packet and have tunneling probabilities of P_{T1}, P_{T21}, and P_{T22}, giving rise to the arbitrary energy distribution at four output ports: A, B, C, and D. (**B**) Output pulse intensity distributions for different coding formats, i.e., from 0001 to 1111. (**C** to **J**) Measured pulse intensity evolutions with coding formats 0001, 0010, 0100, 1000, 0011, 1010, 0111, and 1111, respectively.

driving is removed to separate the two split wave packets. Then, the second and third beam splitters are introduced by applying driving from $m = 46$ to $m = 58$, with the tunneling probabilities denoted by P_{T21} and P_{T22}. To independently set P_{T21} and P_{T22}, we choose different ac-modulation amplitudes and coupler transmittances at the regions $n < 0$ and $n > 0$. Last, at $m = 66$, there exist four output ports—A, B, C, and D—that are uniformly distributed at $n = -54, -14, 26$, and 66 (see note S6). By configuring the splitting ratios of beam splitters, we can encode the distribution of light energy in digital manners, and the four output beams can be treated as four digital bits. Ports A, B, C, and D correspond to the first to fourth digital bits. In Fig. 5B, we illustrate the measured pulse intensity distributions at the output plane for all possible coding formats, i.e., from 0001 to 1111. For formats 0001, 0010, 0100, and 1000, the incident wave packet is arbitrarily routed to one port. For other formats, we equally split the input packet into two, three, and four parts. The highly flexible nature of the synthetic temporal lattice can give rise to a completely dynamical switching of the coding format, which significantly increases the practical value of the LZT-based beam encoding.

The experimental results are shown in Fig. 5 (C to J), where the various panels depict the measured pulse intensity evolutions for certain typical coding formats, including 0001, 0010, 0100, 1000, 0011, 1010, 0111, and 1111. In Fig. 5C, corresponding to 0001, the tunneling probabilities of three beam splitters take values as $P_{T1} = 0$ and $P_{T21} = P_{T22} = 1$. The incident wave packet stays at the negative band after the first LZT and totally goes to the positive one after the second LZT. Consequently, the wave packet comes out from port A, coding the digital format 0001. In Fig. 5D, by changing the tunneling probability of the second beam splitter into $P_{T21} = 0$, the output wave packet is shifted to port B, corresponding to the format 0010. In addition, as shown in Fig. 5 (E and F), we also achieve the encodings of bit sequences 0100 and 1000 using the settings $P_{T1} = 1$, $P_{T21} = P_{T22} = 0$, and $P_{T1} = P_{T21} = P_{T22} = 1$. In Fig. 5 (G and H), the initial packet equally splits into two parts at the second and first splitters, respectively, encoding the formats 0011 and 1010. In Fig. 5I, by setting the splitting ratios as $P_{T1} = 0.33$, $P_{T21} = 0.5$, and $P_{T22} = 0$, we realize an equal splitting of input wave packet at ports A, B, and C, which corresponds to the coding format 0111. If all splitter ratios are tuned to 0.5, then the light energy uniformly distributes at the four output ports, encoding the format 1111 (Fig. 5J).

DISCUSSION

In conclusion, we experimentally demonstrated fully controllable Floquet LZT in synthetic photonic lattices subjected to combined

artificial dc- and ac-driving fields. As compared to most common LZT in crystals with a static Hamiltonian, in the Floquet lattice, we clearly visualize the double tunneling of the wave packet when traveling across the first Brillouin zone and observe a series of cascaded LZT-induced wave splitting events during the evolution, which give rise to multiple trajectories arranged in peculiar regular or irregular patterns. We have shown that a judicious combination of dc- and ac-driving fields and tuning of coupler transmittance can realize a fully controllable and reconfigurable sequence of beam splitters and trajectory paths useful for coherent wave manipulation. As an exciting application, by cascading three LZT beam splitters, we designed and demonstrated a 4-bit temporal beam encoder. Our experiments push the traditional methods of LZT wave control and interference into the Floquet regime, which holds great promise in applications to coherent signal processing, quantum simulation/computation, and quantum metrology (*55*). Because of the reconfigurability of LZT beam splitters, our setup could provide a versatile photonic circuit, enabling linear optical operations required for quantum state preparation and quantum logic (*56*). A dc electric field applied on photons moving on a synthetic and periodically driven lattice would provide a platform for Boson sampling, whereas the introduction of tailored ac fields opens the way to the design of a sequence of reconfigurable quantum gates to implement quantum algorithms. To this aim, one should extend our setting by allowing the coupling T to vary along the transverse n direction as well, so as the scattering matrix of each LZT beam splitter can be tuned independently in both n and m directions. In this way, a rather arbitrary and reconfigurable $N \times N$ linear quantum optical circuit can be realized, which serves as a building block of quantum gates. Last, by introducing gain and loss in the fiber loops, one could explore Floquet LZT in the non-Hermitian regime (*16*, *57*, *58*), where tunneling displays a chiral behavior (*58*), contrary to what happens in Hermitian LZT beam splitters.

MATERIALS AND METHODS

Experimental setup and measurement method

To construct the synthetic temporal lattice, two fiber loops are connected by an optical coupler (shown in fig. S2 of note S2). The length of each fiber loop is ~5 km, and the length difference is ~30 m. To feed the fiber-loop circuit, an optical pulse with a width of ~100 ns is generated through modulating the 1550-nm continuous light with an intensity modulator (IM) and an AWG. To compensate the loss during the pulse circulation, EDFAs are inserted into the loops. To overcome the transient of EDFA, the signal pulses are combined with a pilot light operated at a wavelength of 1530 nm through using a wavelength division multiplexer before entering the EDFA. After exiting the EDFA, the pilot light and spontaneous emission noise are removed by a band-pass filter. In addition, a polarization beam splitter and a subsequent photodiode (PD) are used to monitor the polarization state of the signal pulses. The IMs within the loops serve as optical switches. By alternately switching on and off the short loop at the first 30 to 50 pulse circulations, we can generate a wide wave packet in the circuit (*42*, *48*). In addition, the signal pulses are absorbed after the measurement through switching off the IMs.

To create the artificial dc and ac electric fields, a time-varying phase modulation is imposed using a PM driven by an AWG. Here, the phase modulation is only introduced into the short loop, which has a form $2\phi_u(m)$. The interval between the additional phases in the short and long loops is thus $2\phi_u(m)$, which is actually identical to the one realized through opposite phase modulations (*48*). Because not the phase but the phase difference has physical meaning, such an alternative scheme is hence equivalent to the one mentioned in Results. By programming the output waveform of AWG, we can obtain an effective electric field with an arbitrary driving form.

To capture the pulse dynamics in the circuit, we couple the optical signals out of the loops through optical couplers and detect them with subsequent PDs. By using an oscilloscope, the optical pulse evolutions can be recorded, which produce the LZT dynamics in the m-n temporal lattice.

Supplementary Materials

This PDF file includes:

Notes S1 to S6
Figs. S1 to S5

REFERENCES AND NOTES

1. T. Kato, On the adiabatic theorem of quantum mechanics. *J. Phys. Soc. Japan* **5**, 435–439 (1950).
2. C. Zener, Non-adiabatic crossing of energy levels. *Proc. R. Soc. Lond. A* **137**, 696–702 (1932).
3. M. Grifoni, P. Hänggi, Driven quantum tunneling. *Phys. Rep.* **304**, 229–354 (1998).
4. S. R. Wilkinson, C. F. Bharucha, M. C. Fischer, K. W. Madison, P. R. Morrow, Q. Niu, B. Sundaram, M. G. Raizen, Experimental evidence for non-exponential decay in quantum tunnelling. *Nature* **387**, 575–577 (1997).
5. A. Zenesini, H. Lignier, G. Tayebirad, J. Radogostowicz, D. Ciampini, R. Mannella, S. Wimberger, O. Morsch, E. Arimondo, Time-resolved measurement of Landau-Zener tunneling in periodic potentials. *Phys. Rev. Lett.* **103**, 090403 (2009).
6. A. Sibille, J. F. Palmier, F. Laruelle, Zener interminiband resonant breakdown in superlattices. *Phys. Rev. Lett.* **80**, 4506–4509 (1998).
7. B. Rosam, D. Meinhold, F. Löser, V. G. Lyssenko, S. Glutsch, F. Bechstedt, F. Rossi, K. Köhler, K. Leo, Field-induced delocalization and Zener breakdown in semiconductor superlattices. *Phys. Rev. Lett.* **86**, 1307–1310 (2001).
8. D. M. Berns, W. D. Oliver, S. O. Valenzuela, A. V. Shytov, K. K. Berggren, L. S. Levitov, T. P. Orlando, Coherent quasiclassical dynamics of a persistent current qubit. *Phys. Rev. Lett.* **97**, 150502 (2006).
9. O. V. Ivakhnenko, S. N. Shevchenko, F. Nori, Nonadiabatic Landau-Zener-Stückelberg-Majorana transitions, dynamics, and interference. *Phys. Rep.* **995**, 1–89 (2023).
10. D. L. Campbell, Y.-P. Shim, B. Kannan, R. Winik, D. K. Kim, A. Melville, B. M. Niedzielski, J. L. Yoder, C. Tahan, S. Gustavsson, W. D. Oliver, Universal nonadiabatic control of small-gap superconducting qubits. *Phys. Rev. X* **10**, 041051 (2020).
11. A. Fratalocchi, G. Assanto, All-optical Landau-Zener tunneling in waveguide arrays. *Opt. Express* **14**, 2021–2026 (2006).
12. H. Trompeter, T. Pertsch, F. Lederer, D. Michaelis, U. Streppel, A. Bräuer, U. Peschel, Visual observation of Zener tunneling. *Phys. Rev. Lett.* **96**, 023901 (2006).
13. F. Dreisow, A. Szameit, M. Heinrich, T. Pertsch, S. Nolte, A. Tünnermann, S. Longhi, Bloch-Zener oscillations in binary superlattices. *Phys. Rev. Lett.* **102**, 076802 (2009).
14. Y.-J. Chang, Y.-H. Lu, Y.-Y. Yang, Y. Wang, W.-H. Zhou, X.-W. Wang, X.-M. Jin, Inhibition and reconstruction of Zener tunneling in photonic honeycomb lattices. *Adv. Mater.* **34**, 2110044 (2022).
15. Y. Sun, D. Leykam, S. Nenni, D. Song, H. Chen, Y. D. Chong, Z. Chen, Observation of valley Landau-Zener-Bloch oscillations and pseudospin imbalance in photonic graphene. *Phys. Rev. Lett.* **121**, 033904 (2018).
16. S. Xia, C. Danieli, Y. Zhang, X. Zhao, L. Tang, H. Lu, D. Li, D. Song, Z. Chen, Higher-order exceptional point and Landau-Zener Bloch oscillations in driven non-Hermitian photonic Lieb lattices. *APL Photonics* **6**, 126106 (2021).
17. Y. Long, J. Ren, Topological Landau-Zener Bloch oscillations in photonic Floquet Lieb lattices. arXiv:1706.01107 (2017); https://doi.org/10.48550/arXiv.1706.01107.
18. J. Schwinger, On gauge invariance and vacuum polarization. *Phys. Rev.* **82**, 664–679 (1951).

19. B. Damski, The simplest quantum model supporting the Kibble-Zurek mechanism of topological defect production: Landau-Zener transitions from a new perspective. *Phys. Rev. Lett.* **95**, 035701 (2005).
20. B. M. Breid, D. Witthaut, H. J. Korsch, Manipulation of matter waves using Bloch and Bloch-Zener oscillations. *New J. Phys.* **9**, 62 (2007).
21. S. Longhi, Bloch-Zener quantum walk. *J. Phys. B: At. Mol. Opt. Phys.* **45**, 225504 (2012).
22. S. J. Park, H. K. Andersen, S. Mai, J. Arlt, J. F. Sherson, Dynamical control of matter-wave splitting using time-dependent optical lattices. *Phys. Rev. A* **85**, 033626 (2012).
23. D. M. Berns, M. S. Rudner, S. O. Valenzuela, K. K. Berggren, W. D. Oliver, L. S. Levitov, T. P. Orlando, Amplitude spectroscopy of a solid-state artificial atom. *Nature* **455**, 51–57 (2008).
24. M. S. Rudner, N. H. Lindner, E. Berg, M. Levin, Anomalous edge states and the bulk-edge correspondence for periodically driven two-dimensional systems. *Phys. Rev. X* **3**, 031005 (2013).
25. N. Goldman, J. Dalibard, Periodically driven quantum systems: Effective Hamiltonians and engineered gauge fields. *Phys. Rev. X* **4**, 031027 (2014).
26. T. Oka, S. Kitamura, Floquet engineering of quantum materials. *Annu. Rev. Condens. Matter Phys.* **10**, 387–408 (2019).
27. L. J. Maczewsky, J. M. Zeuner, S. Nolte, A. Szameit, Observation of photonic anomalous Floquet topological insulators. *Nat. Commun.* **8**, 13756 (2017).
28. J. Zhang, P. W. Hess, A. Kyprianidis, P. Becker, A. Lee, J. Smith, G. Pagano, I. D. Potirniche, A. C. Potter, A. Vishwanath, N. Y. Yao, C. Monroe, Observation of a discrete time crystal. *Nature* **543**, 217–220 (2017).
29. X. Mi, M. Ippoliti, C. Quintana, A. Greene, Z. Chen, J. Gross, F. Arute, K. Arya, J. Atalaya, R. Babbush, J. C. Bardin, J. Basso, A. Bengtsson, A. Bilmes, A. Bourassa, L. Brill, M. Broughton, B. B. Buckley, D. A. Buell, B. Burkett, N. Bushnell, B. Chiaro, R. Collins, W. Courtney, D. Debroy, S. Demura, A. R. Derk, A. Dunsworth, D. Eppens, C. Erickson, E. Farhi, A. G. Fowler, B. Foxen, C. Gidney, M. Giustina, M. P. Harrigan, S. D. Harrington, J. Hilton, A. Ho, S. Hong, T. Huang, A. Huff, W. J. Huggins, L. B. Ioffe, S. V. Isakov, J. Iveland, E. Jeffrey, Z. Jiang, C. Jones, D. Kafri, T. Khattar, S. Kim, A. Kitaev, P. V. Klimov, A. N. Korotkov, F. Kostritsa, D. Landhuis, P. Laptev, J. Lee, K. Lee, A. Locharla, E. Lucero, O. Martin, J. R. McClean, T. McCourt, M. McEwen, K. C. Miao, M. Mohseni, S. Montazeri, W. Mruczkiewicz, O. Naaman, M. Neeley, C. Neill, M. Newman, M. Y. Niu, T. E. O'Brien, A. Opremcak, E. Ostby, B. Pato, A. Petukhov, N. C. Rubin, D. Sank, K. J. Satzinger, V. Shvarts, Y. Su, D. Strain, M. Szalay, M. D. Trevithick, B. Villalonga, T. White, Z. J. Yao, P. Yeh, J. Yoo, A. Zalcman, H. Neven, S. Boixo, V. Smelyanskiy, A. Megrant, J. Kelly, Y. Chen, S. L. Sondhi, R. Moessner, K. Kechedzhi, V. Khemani, P. Roushan, Time-crystalline eigenstate order on a quantum processor. *Nature* **601**, 531–536 (2022).
30. L. Morales-Molina, S. Flach, J. B. Gong, Quantum ratchet control—Harvesting on Landau-Zener transitions. *Europhys. Lett.* **83**, 40005 (2008).
31. K. Uchida, S. Kusaba, K. Nagai, T. N. Ikeda, K. Tanaka, Diabatic and adiabatic transitions between Floquet states imprinted in coherent exciton emission in monolayer WSe2. *Sci. Adv.* **8**, eabq7281 (2022).
32. T. N. Ikeda, S. Tanaka, Y. Kayanuma, Floquet-Landau-Zener interferometry: Usefulness of the Floquet theory in pulse-laser-driven systems. *Phys. Rev. Res.* **4**, 033075 (2022).
33. Q. Gao, Q. Niu, Floquet-Bloch oscillations and intraband Zener tunneling in an oblique spacetime crystal. *Phys. Rev. Lett.* **127**, 036401 (2021).
34. M. Genske, W. Alt, A. Steffen, A. H. Werner, R. F. Werner, D. Meschede, A. Alberti, Electric quantum walks with individual atoms. *Phys. Rev. Lett.* **110**, 190601 (2013).
35. A. D'Errico, R. Barboza, R. Tudor, A. Dauphin, P. Massignan, L. Marrucci, F. Cardano, Bloch-Landau-Zener dynamics induced by a synthetic field in a photonic quantum walk. *APL Photonics* **6**, 020802 (2021).
36. G. Milione, T. A. Nguyen, J. Leach, D. A. Nolan, R. R. Alfano, Using the nonseparability of vector beams to encode information for optical communication. *Opt. Lett.* **40**, 4887–4890 (2015).
37. Y. Zhao, J. Wang, High-base vector beam encoding/decoding for visible-light communications. *Opt. Lett.* **40**, 4843–4846 (2015).
38. S. Chen, S. Li, Y. Zhao, J. Liu, L. Zhu, A. Wang, J. Du, L. Shen, J. Wang, Demonstration of 20-gbit/s high-speed Bessel beam encoding/decoding link with adaptive turbulence compensation. *Opt. Lett.* **41**, 4680–4683 (2016).
39. A. Regensburger, C. Bersch, B. Hinrichs, G. Onishchukov, A. Schreiber, C. Silberhorn, U. Peschel, Photon propagation in a discrete fiber network: An interplay of coherence and losses. *Phys. Rev. Lett.* **107**, 233902 (2011).
40. A. Regensburger, C. Bersch, M. A. Miri, G. Onishchukov, D. N. Christodoulides, U. Peschel, Parity-time synthetic photonic lattices. *Nature* **488**, 167–171 (2012).
41. M. Wimmer, M.-A. Miri, D. Christodoulides, U. Peschel, Observation of Bloch oscillations in complex PT-symmetric photonic lattices. *Sci. Rep.* **5**, 17760 (2015).
42. M. Wimmer, H. M. Price, I. Carusotto, U. Peschel, Experimental measurement of the Berry curvature from anomalous transport. *Nat. Phys.* **13**, 545–550 (2017).
43. S. Wang, C. Qin, B. Wang, P. Lu, Discrete temporal Talbot effect in synthetic mesh lattices. *Opt. Express* **26**, 19235–19246 (2018).
44. S. Wang, B. Wang, P. Lu, PT-symmetric Talbot effect in a temporal mesh lattice. *Phys. Rev. A* **98**, 043832 (2018).
45. S. Weidemann, M. Kremer, T. Helbig, T. Hofmann, A. Stegmaier, M. Greiter, R. Thomale, A. Szameit, Topological funneling of light. *Science* **368**, 311–314 (2020).
46. S. Weidemann, M. Kremer, S. Longhi, A. Szameit, Coexistence of dynamical delocalization and spectral localization through stochastic dissipation. *Nat. Photonics* **15**, 576–581 (2021).
47. M. Wimmer, M. Monika, I. Carusotto, U. Peschel, H. M. Price, Superfluidity of light and its breakdown in optical mesh lattices. *Phys. Rev. Lett.* **127**, 163901 (2021).
48. S. Wang, C. Qin, W. Liu, B. Wang, F. Zhou, H. Ye, L. Zhao, J. Dong, X. Zhang, S. Longhi, P. Lu, High-order dynamic localization and tunable temporal cloaking in ac-electric-field driven synthetic lattices. *Nat. Commun.* **13**, 7653 (2022).
49. S. Weidemann, M. Kremer, S. Longhi, A. Szameit, Topological triple phase transition in non-Hermitian Floquet quasicrystals. *Nature* **601**, 354–359 (2022).
50. K. Fang, Z. Yu, S. Fan, Photonic Aharonov-Bohm effect based on dynamic modulation. *Phys. Rev. Lett.* **108**, 153901 (2012).
51. C. Qin, L. Yuan, B. Wang, S. Fan, P. Lu, Effective electric-field force for a photon in a synthetic frequency lattice created in a waveguide modulator. *Phys. Rev. A* **97**, 063838 (2018).
52. C. Qin, F. Zhou, Y. Peng, D. Sounas, X. Zhu, B. Wang, J. Dong, X. Zhang, A. Alù, P. Lu, Spectrum control through discrete frequency diffraction in the presence of photonic gauge potentials. *Phys. Rev. Lett.* **120**, 133901 (2018).
53. J. R. Petta, H. Lu, A. C. Gossard, A coherent beam splitter for electronic spin states. *Science* **327**, 669–672 (2010).
54. C. M. Quintana, K. D. Petersson, L. W. McFaul, S. J. Srinivasan, A. A. Houck, J. R. Petta, Cavity-mediated entanglement generation via Landau-Zener interferometry. *Phys. Rev. Lett.* **110**, 173603 (2013).
55. Z.-E. Su, Y. Li, P. P. Rohde, H.-L. Huang, X.-L. Wang, L. Li, N.-L. Liu, J. P. Dowling, C.-Y. Lu, J.-W. Pan, Multiphoton interference in quantum fourier transform circuits and applications to quantum metrology. *Phys. Rev. Lett.* **119**, 080502 (2017).
56. E. Knill, R. Laflamme, G. J. Milburn, A scheme for efficient quantum computation with linear optics. *Nature* **409**, 46–52 (2001).
57. X. Shen, F. Wang, Z. Li, Z. Wu, Landau-Zener-Stückelberg interferometry in PT-symmetric non-Hermitian models. *Phys. Rev. A* **100**, 062514 (2019).
58. S. Longhi, Non-Bloch-band collapse and chiral Zener tunneling. *Phys. Rev. Lett.* **124**, 066602 (2020).

Acknowledgments

Funding: This work was supported by the National Natural Science Foundation of China (nos. 11974124, 12204185, 12147151, and 12021004). **Author contributions:** B.W. conceived the idea. S.W. designed and performed the experiment. S.W. and C.Q. analyzed the data. C.Q., B.W., and S.L. provided the theoretical support. B.W. and P.L. supervised the project. All authors contributed to the discussion of the results and writing of the manuscript. **Competing interests:** The authors declare that they have no competing interests. **Data and materials availability:** All data needed to evaluate the conclusions in the paper are present in the paper and/or the Supplementary Materials.

Submitted 6 February 2023
Accepted 31 March 2023
Published 3 May 2023
10.1126/sciadv.adh0415

ScienceAdvances

Photonic Floquet Landau-Zener tunneling and temporal beam splitters

Shulin Wang, Chengzhi Qin, Lange Zhao, Han Ye, Stefano Longhi, Peixiang Lu, and Bing Wang

Sci. Adv., **9** (18), eadh0415.
DOI: 10.1126/sciadv.adh0415